Gravitational Waves in the Abelian Higgs Model

Bachelorarbeit

zur Erlangung des akademischen Grades
Bachelor of Science (B.Sc.) in Physik am
Institut für Theoretische Physik (ITP) der
Goethe-Universität Frankfurt am Main

vorgelegt von
Rebecca Baumann
am 11. Oktober 2023

Erstgutachterin: Prof. Dr. Laura Sagunski
Zweitgutachter: Dr. Philipp Schicho

Selbstständigkeitserklärung

Hiermit erkläre ich, dass ich die Arbeit selbstständig und ohne Benutzung anderer als der angegebenen Quellen und Hilfsmittel verfasst habe. Alle Stellen der Arbeit, die wörtlich oder sinngemäß aus Veröffentlichungen oder aus anderen fremden Texten entnommen wurden, sind von mir als solche kenntlich gemacht worden. Ferner erkläre ich, dass die Arbeit nicht – auch nicht auszugsweise – für eine andere Prüfung verwendet wurde.

Frankfurt a.M., den 11. Oktober 2023

Rebecca Baumann

Rebecca Baumann
Institute of Theoretical Physics
Max-von-Laue-Str. 1
60438 Frankfurt am Main, Germany
Goethe University

Abstract

In this thesis, we study the phase structure of the Abelian Higgs model and determine regions of the parameter space that exhibit first-order phase transitions. For this purpose, we construct the thermal effective potential up to one-loop order and examine its thermal evolution for the emergence of a thermal barrier. Furthermore, we compute the stochastic gravitational wave spectra and draw conclusions if such signals are detectable by future space-based gravitational wave observatories and pulsar timing arrays.

TABLE OF CONTENTS

CHAPTER 1
INTRODUCTION

If we look deeper and deeper into space it is well known that we also look back in time. However, we eventually reach a natural barrier: the **cosmic microwave background** (CMB). The early universe – being of particular interest for high-energy particle physics – would therefore remain hidden to us if light was our only way to make observations. That is when **gravitational waves** (GWs) come into play. Analogous to the CMB, the superposition of many independent GW generating processes in the early universe results in a **stochastic gravitational wave background** (SGWB) observable today. Predicted by Albert Einstein in 1916 [13][14], the first GW signal was detected a century later [20], marking the emergence of a new field of research. To this day, GWs offer the opportunity to study problems involving energy scales predominant in the early universe but inaccessible to laboratories on earth. These problems include *Baryogenesis*, *Dark Matter*, the *Flatness* and the *Horizon problem*, along with the *Hierarchy problem*, amongst others. The **Standard Model of particle physics** (SM) fails to explain these phenomena which is why researchers are looking for extensions.

In this thesis, we extend the SM by a new Abelian $U(1)$ gauge symmetry, known as the **Abelian Higgs model** [35][38]. The theory introduces a *dark photon*, behaving like a massive particle when interacting with a singlet Higgs-like scalar field. We will investigate if the thermal effective potential enables a **first order phase transition** (FOPT) and compute the corresponding GW spectrum. We compare our data with the detection range of various planned (or proposed) space-based observatories: the Laser Interferometer Space Antenna (LISA) [3][21], the Big Bang Observer (BBO) [31], μAres [19] and the Einstein Telescope (ET) [23]. We also check if our results could potentially be registered with **pulsar timing arrays** (PTAs) which are a set of millisecond pulsars whose deviations from their proper frequency are used to detect spacetime curvatures. Therefore, we compare our results with the recent data from the NANOGrav 15-year Data Set [18].

CHAPTER 2
THEORY AND BACKGROUND

2.1 Cosmology

The following introduction is based on the lecture notes of Daniel Baumann [4, 5]. It should be noted that we use natural units in this thesis, i.e. $\hbar = c = 1$.

2.1.1 Geometry and dynamics of spacetime

The assumption that the universe is homogeneous and isotropic on large scales is called the **cosmological principle**. In agreement with this, the 4-dimensional spacetime can be foliated into time-ordered 3-dimensional hypersurfaces, which are also homogeneous and isotropic. Taking into account the expansion of the universe, we obtain the **Friedmann-Robertson-Walker** (FRW) metric. In polar coordinates, it reads

$$ds^2 = -dt^2 + a^2(t)\Big[\frac{dr^2}{1 - kr^2/R_0^2} + r^2 d\Omega^2\Big],\tag{2.1}$$

where R_0 is the curvature scale and $d\Omega^2 \equiv d\theta^2 + \sin^2(\theta)d\phi^2$. In particular, the scale factor $a(t)$ is introduced as well as the curvature parameter $k \in \{0, +1, -1\}$ for flat, positively (spherical) and negatively (hyperbolic) curved space, respectively.

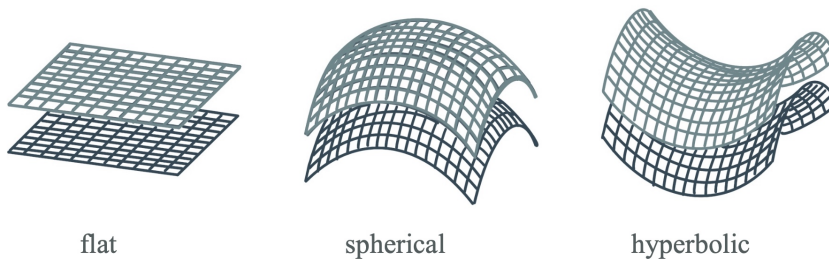flat   spherical   hyperbolic

Fig. 2.1: Curvature of spacetime for $k = 0$ (left), $k = +1$ (center), $k = -1$ (right).

Proceeding from the metric, we now want to analyze the dynamics of spacetime. For this we examine how the scale factor $a(t)$ evolves with time. We apply the **Einstein equation**,

$$G_{\mu\nu} = 8\pi G T_{\mu\nu},\tag{2.2}$$

to the FRW metric. The above expression is actually a set of ten nonlinear differential equations. It states the principle of spacetime curvature under the influence of energy and matter. It comes with the metric-dependent Einstein tensor $G_{\mu\nu}$, the gravitational constant G and the energy-momentum tensor $T_{\mu\nu}$. The latter is a perfect fluid in the FRW metric[1]:

$$T_{\mu\nu} = \text{diag}(\rho, P, P, P),\tag{2.3}$$

with energy density ρ and pressure P.

The zeroth component of the Einstein equation yields the **Friedmann equation**. It provides a differential equation for the scale factor $a(t)$ whereas the **second Friedmann equation** yields an acceleration equation for $a(t)$ and results from the spatial components of the Einstein equation:

$$G_{00} = 8\pi G T_{00} \qquad \Rightarrow \qquad \left(\frac{\dot{a}}{a}\right)^2 = \frac{8\pi G}{3}\rho - \frac{k/R_0}{a^2},\tag{2.4a}$$

$$G_{ij} = 8\pi G T_{ij} \qquad \Rightarrow \qquad \frac{\ddot{a}}{a} = -\frac{4\pi G}{3}(\rho + 3P).\tag{2.4b}$$

In the literature, the **Hubble parameter**:

$$H \equiv \frac{\dot{a}}{a},\tag{2.5}$$

denotes the expansion rate of the universe. Today's expansion rate is given by the **Hubble constant** $H_0 \approx 70\text{km/sec/Mpc}$ [25]. Additionally, one can define the critical energy density today (for a flat universe [25], cf. Fig. 2.1, left):

$$\rho_{\text{crit},0} \equiv \frac{3H_0^3}{8\pi G}.\tag{2.6}$$

Information about the evolution of density ρ and pressure P provides the continuity equation $\nabla_\mu T^{\mu\nu} = 0$. When formulated in the FRW metric, it looks as follows:

$$\dot{\rho} + 3\frac{\dot{a}}{a}(\rho + P) = 0.\tag{2.7}$$

The constant equation of state,

$$w = \frac{P}{\rho},\tag{2.8}$$

provides a relation between density ρ and pressure P. Then, using Eq. (2.7), we obtain the three forms of energy in the ΛCDM-model [36]:

$$\frac{\dot{\rho}}{\rho} = -3(1+w) \quad \Rightarrow \quad \rho = \frac{\rho_0}{a^{3(1+w)}} \propto \begin{cases} a^{-3} & \text{pressureless matter,} \\ a^{-4} & \text{radiation,} \\ a^0 & \text{dark energy,} \end{cases}\tag{2.9}$$

---

[1]We assume the fluid to be in rest in the considered frame of the universe.
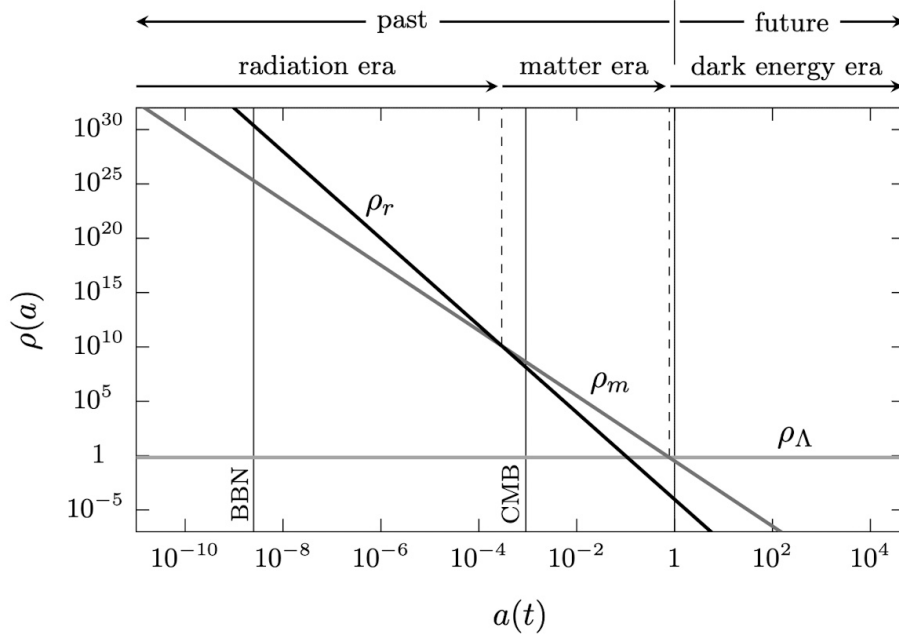
Fig. 2.2: Three different stages of evolution: First, the radiation dominated era ($\rho \propto a^{-4}$) during which Big Bang nucleosynthesis (BBN) occurs and which lasts until the formation of the CMB, followed by the matter dominated era ($\rho \propto a^{-3}$). Nowadays, the energy density of the universe is dark energy dominated ($\rho \propto a^0$). Figure adopted from [5]

where the integration constant ρ_0 is the energy density today when we set $a(t_0) \equiv 1$ by convention. In the case of dark energy, the energy density remains constant with an expanding universe, resulting in a negative pressure.

Often times, in order to differ between the different forms of energy in the universe, Eq. (2.4a) is expressed the following way:

$$\frac{H^2}{H_0^2} = \frac{\Omega_m}{a^3} + \frac{\Omega_r}{a^4} + \Omega_\Lambda \,, \tag{2.10}$$

with

$$\Omega_i \equiv \frac{\rho_i}{\rho_{\text{crit}}}, \quad i = \begin{cases} \text{m} & \text{matter,} \\ \text{r} & \text{radiation,} \\ \Lambda & \text{dark energy.} \end{cases} \tag{2.11}$$

The values are [24][25]

$$\Omega_m = 0.32 \,, \qquad \Omega_r = 8.99 \times 10^{-5}, \qquad \Omega_\Lambda = 0.68 \,, \tag{2.12}$$

where Ω_m= 0.05, 0.27 for visible and dark matter, respectively. Thus, the question about the nature of dark matter and dark energy is also a fundamental question about the nature of the universe as they make up 95% of the total energy.

2.1.2   Gravitational radiation

Analogous to electromagnetic waves as solutions of the Maxwell equations, $\partial_\mu F^{\mu\nu} = J^\nu$, GWs solve the Einstein equations (cf. Eq. (2.2)). They are to be understood as ripples in space-time, which propagate unhindered in space with the speed of light.

Linearized theory in vacuum

We consider a small perturbation $|h_{\mu\nu}| \ll 1$ around the flat Minkowskian metric $\eta_{\mu\nu} = \mathrm{diag}(-1, +1, +1, +1)$,

$$g_{\mu\nu} = \eta_{\mu\nu} + h_{\mu\nu}\,, \tag{2.13}$$

and are free to lower and raise indices with $\eta_{\mu\nu}$ instead of $g_{\mu\nu}$ since all quadratic or higher order terms can be neglected [42]. Moreover, we introduce the *trace-reversed* metric perturbation:

$$\bar{h}_{\mu\nu} \equiv h_{\mu\nu} - \frac{1}{2}h\eta_{\mu\nu}\,, \tag{2.14}$$

where $h = \eta_{\mu\nu}h^{\mu\nu}$. The Einstein equations are gauge invariant and do not change under infinitesimal coordinate transformations. Thus, nothing prevents us from choosing a convenient gauge. Just as Lorentz gauge simplifies the Maxwell equations in such a way that they reduce to wave equations, we want to achieve the same in linearized gravity by introducing the *de Donder gauge*:

$$\partial^\mu h_{\mu\nu} - \frac{1}{2}\partial_\nu h = 0\,. \tag{2.15}$$

With this gauge and using the *trace-reversed* metric perturbation, Eq. (2.2) simplifies to a series of decoupled linear wave equations that read in vacuum ($T_{\mu\nu} = 0$) [42]:

$$\Box\bar{h}_{\mu\nu} = 0\,. \tag{2.16}$$

Their solutions are plane waves [5]:

$$\bar{h}_{\mu\nu} = \mathrm{Re}\big(H_{\mu\nu}\mathrm{e}^{ik_\lambda x^\lambda}\big)\,, \tag{2.17}$$

with the complex polarization matrix $H_{\mu\nu}$ and the wavevector $k^\mu = (\omega, \mathbf{k})$ with frequency ω and three-dimensional wavevector $\mathbf{k}$. In order to solve Eq. (2.17), GWs need to propagate with the speed of light.[2]

We will now present a common way to reduce the number of independent polarizations from 10 to 2: The *de Donder* gauge requires transverse polarization to the direction of propagation since it indicates that

$$k^\mu H_{\mu\nu} = 0\,, \tag{2.18}$$

reducing the polarizations from 10 to 6.

---

[2]That is because $\Box\bar{h}_{\mu\nu} = -(k_\mu k^\mu)\bar{h}_{\mu\nu} \;\Leftrightarrow\; k_\mu k^\mu = 0 \;\Rightarrow\; \omega \overset{!}{=} \pm|\mathbf{k}|$.

Considering a second gauge transformation,

$$\bar{h}_{\mu\nu} \to \bar{h}_{\mu\nu} + \partial_\mu \xi_\nu + \partial_\nu \xi_\mu - \partial^\sigma \xi_\sigma \eta_{\mu\nu} \,, \tag{2.19}$$

and demanding

$$\Box \xi_\mu = 0 \quad \Rightarrow \quad \xi_\mu = \lambda_\mu \mathrm{e}^{ik_\lambda x^\lambda} \tag{2.20}$$

yields the following shift in the polarization matrix while still describing the same GW [5]:

$$H_{\mu\nu} \to H_{\mu\nu} + i(k_\mu \lambda_\nu + k_\nu \lambda_\mu - k^\sigma \lambda_\sigma \eta_{\mu\nu}) \,. \tag{2.21}$$

This leads to the **transverse traceless gauge** (TTG), where

$$H_{0\mu} = 0 \,, \qquad H^\mu_\mu = 0 \qquad \text{and} \qquad \bar{h}_{\mu\nu} = h_{\mu\nu} \,. \tag{2.22}$$

We are now left with 2 independent polarizations. For a GW that propagates in z-direction, the polarization matrix looks as follows [5]:

$$H_{\mu\nu} = \begin{pmatrix} 0 & 0 & 0 & 0 \\ 0 & H_+ & H_\times & 0 \\ 0 & H_\times & -H_+ & 0 \\ 0 & 0 & 0 & 0 \end{pmatrix}, \tag{2.23}$$

for +- and ×-polarization.

How these polarizations affect particles becomes clear when one considers a ring of particles under the influence of a GW. For this, the dynamics of a vector B^μ which reaches from the center of the ring to any particle of the considered system is relevant.

The **geodesic deviation equation**

$$\frac{d^2 B^\mu}{dt^2} = \frac{1}{2} \frac{d^2 h^\mu_\rho}{dt^2} B^\rho \qquad (h_{\mu 0} = 0) \,, \tag{2.24}$$

yields two equations of motion for B^1 and B^2 whose solutions (for small H_+ and $H_\times$, respectively) read [5]:

$$B^1(t) = B^1(0)\Big(1 + \frac{1}{2} H_+ \mathrm{e}^{iwt} + \dots \Big)\,, \tag{2.25a}$$

$$B^2(t) = B^2(0)\Big(1 - \frac{1}{2} H_+ \mathrm{e}^{iwt} + \dots \Big)\,, \tag{2.25b}$$

where $B^1(0)^2 + B^2(0)^2 = R^2$ is the radius of the particle ring which is periodically distorted to an ellipse at +-polarization (see Fig. 2.3).

Considering small $H_\times$ yields [5]:

$$B^1(t) = B^1(0) + \frac{1}{2} B^2(0) H_\times \mathrm{e}^{i\omega t} + \dots \,, \tag{2.26a}$$

$$B^2(t) = B^2(0) + \frac{1}{2} B^1(0) H_\times \mathrm{e}^{i\omega t} + \dots \,, \tag{2.26b}$$

which can be rewritten as

$$B^1(t) \pm B^2(t) = [B^1(0) \pm B^2(0)]\left(1 \pm \frac{1}{2}H_\times e^{i\omega t} + \dots\right), \qquad (2.27)$$

resulting in a similar distortion as in the case of +-polarization but rotated by 45°. The resulting deformation of the considered particle ring under the influence of a GW with different polarizations is illustrated in Fig. 2.3.
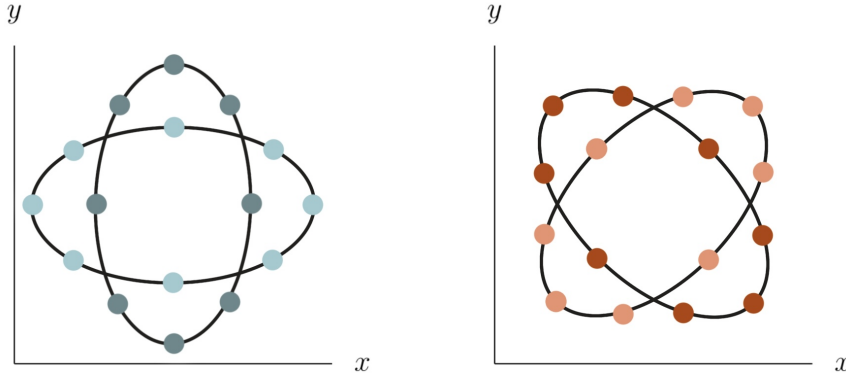

Fig. 2.3: Deformation of a particle ring in the x-y-plane for a GW propagating in z-direction. Left: +-polarization. Right: ×-polarization.

Detection of gravitational waves

In 1887, A. A. Michelson and E. W. Morley performed an experiment to confirm the dependence of the speed of light on the earth's direction of motion, based on the assumption that it moves through a so-called luminiferous ether [37]. The measurements were made using an Michelson interferometer which is a construction of two crossing, orthogonal arms of the same length. A monochromatic laser beam is split so that both light beams pass simultaneously through one of the arms and are reflected at its end. The returning beams hit a detector which will register interference in case of varying runtimes. Michelson and Morley expected to observe an interference pattern resulting from an anisotropy of the speed of light. However, they could not register any directional variations that could be attributed to a relative motion of the earth and the ether.[3]

Today, Michelson interferometers are applied for the detection of phenomena that *seem* to influence light in such a way that one could believe it is due to a direction-dependent speed. However, it is spacetime itself that is affected by the passage of a GW, resulting in a runtime difference of two light beams.

For simplicity, assume that one GW interfereometer arm lies on the x-axis with length $L = x$ and the GW moves with +-polarization in z-direction. The time t_{return} taken by the returning light beam can be easily calculated in flat Minkowskian metric in the following way [42]:

$$t_{\text{return}} = t + L + \frac{1}{2}\left[\underbrace{\int_0^L h_+(t+x)dx}_{\text{variations before reflection}} + \underbrace{\int_0^L h_+(t+x+L)dx}_{\text{variations after reflection}}\right], \qquad (2.28)$$

where $h_+ = \mathcal{A}H_+\mathrm{e}^{-i\omega(t-z)}$ with amplitude $\mathcal{A}$ and the start time t. Temporal fluctuations therefore occur with the rate [42]

$$\frac{dt_{\text{return}}}{dt} = 1 + \frac{1}{2}\big[h_+(t+2L) - h_+(t)\big] . \qquad (2.29)$$

In general, the changes in length δL of the interferometer arms are [5]:

$$\frac{\delta L}{L} \approx \frac{H_{+,\times}}{2} . \qquad (2.30)$$

---

[3]That is, of course, because such an ether does not exist.

Linearized theory in matter

Next, we consider the so-called *inhomogeneous wave equation* for GWs resulting from a source of matter in a certain region Σ,

$$\Box \bar{h}_{\mu\nu} = -16\pi G T_{\mu\nu} \; . \tag{2.31}$$

The solution is given by [5]

$$\bar{h}_{\mu\nu}(t, \mathbf{x}) = 4G \int_{\Sigma} d^3y \; \frac{T_{\mu\nu}(t_r, \mathbf{y})}{|\mathbf{x} - \mathbf{y}|} \; , \tag{2.32}$$

where $t_r = t - |\mathbf{x} - \mathbf{y}|$ denotes the "retarded time" which takes into account that the influence of matter at location $\mathbf{y}$ on the gravitational field $\bar{h}_{\mu\nu}(t, \mathbf{x})$ cannot instantaneously affect a location $\mathbf{x}$ since GWs propagate at the speed of light.

Let d be the size of the source at large distance $r = |\mathbf{x}| \gg d$. The divisor in the integral from Eq. (2.32) then changes as shown below:

$$|\mathbf{x} - \mathbf{y}| = r - \frac{\mathbf{x} \cdot \mathbf{y}}{r} + \dots \qquad \Rightarrow \qquad \frac{1}{|\mathbf{x} - \mathbf{y}|} = \frac{1}{r} + \frac{\mathbf{x} \cdot \mathbf{y}}{r^3} + \dots \; . \tag{2.33}$$

This also affects the energy-momentum tensor:

$$T_{\mu\nu}(t_r, \mathbf{y}) = T_{\mu\nu}(t - r, \mathbf{y}) + \frac{d}{dr} T_{\mu\nu}(t - r, \mathbf{y}) \frac{\mathbf{x} \cdot \mathbf{y}}{r} + \dots \; . \tag{2.34}$$

The gravitational field at large distance from the source then reads (keeping only linear terms of $T_{\mu\nu}$) [5]:

$$\bar{h}_{\mu\nu}(t, \mathbf{x}) \approx \frac{4G}{r} \int_{\Sigma} d^3y \; T_{\mu\nu}(t - r, \mathbf{y}) \; . \tag{2.35}$$

The spatial solutions reveal the second-order derivative of the source's **energy quadrupole moment** I_{ij}:

$$\bar{h}_{ij}(t, \mathbf{x}) = \frac{2G}{r} \frac{d^2 I_{ij}}{dt^2}(t_r) \; , \tag{2.36}$$

with

$$I_{ij}(t_r) \equiv \int_{\Sigma} d^3y \; T^{00}(t_r, \mathbf{y}) y_i y_j \; . \tag{2.37}$$

Hence, Gws are generated by the energy quadrupole moment of the source changing with time.

2.2 Cosmological phase transitions

Cosmological **phase transitions** (PTs) occur between states of true (stable) and false (metastable) vacuum and have profound effects on the dynamics of the universe as well as on particle physics. However, their concept is similar to that of conventional phase transitions, e.g. the transition from liquid to gas. In the case of FOPT, bubbles of the new stable phase form and then expand, somewhat like boiling water[4].
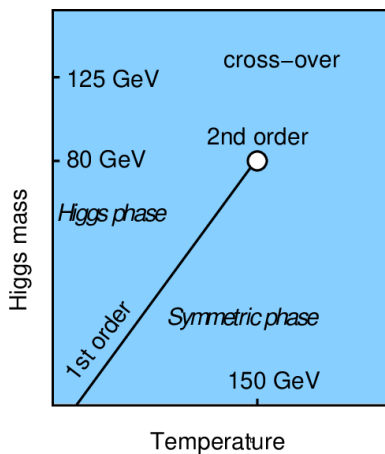

Fig. 2.4: The SM phase diagram. Taken from [30]

The phase diagram of the SM is given in Fig. 2.4 and will be briefly discussed at this point in preparation for the discussions in the sections below.

For Higgs masses below $m_H \sim 75$ GeV, the SM exhibits a first-order phase transition. At some critical temperature T_c, the scalar field ϕ tunnels to the Higgs phase. Bubbles of the new stable phase ($\phi \neq 0$) form and expand into the metastable symmetric phase ($\phi = 0$). Their collision will generate a series of events that result in a stochastic GW signal (see Sec. 2.2.4).

The SM undergoes a second-order PT for Higgs masses around $m_H \sim 80$ GeV. In that case, no latent heat is required and consequently no GWs are generated. For larger Higgs masses, the SM has no PT but a cross-over and the symmetric phase smoothly changes to the Higgs phase. The latent heat is zero.

2.2.1 Phase transitions in thermal field theory

The following overview on perturbative thermal field theory follows [33].

At zero temperature, relativistic quantum mechanics is mathematically described by **quantum field theory**[5] (QFT). One important object of this theory is the Lorentz invariant Lagrangian density $\mathcal{L}$ which contains the kinetic terms and interactions of a system. When integrating the Lagrangian density, we obtain the action S:

$$S = \int \mathcal{L}(x) \, d^4x \ . \tag{2.38}$$

The principle of least action $\delta S = 0$ states that small variations of the quantum fields do not affect S. This leads to the equations of motion in QFT, similarily as in

---

[4]Where in our case, bubbles of the stable phase appear and grow through cooling, see Sec. 3.1. Moreover, latent heat is released during the cooling whereas in the case of boiling water, latent heat is converted into the kinetic energy of the molecules.

[5]Here, a quantum field is represented by an infinite set of harmonic oscillators.

classical mechanics. It also means that, for the ground state (vacuum), the potential V is minimal.

At finite temperature, the partition function $\mathcal{Z}$ is of particular interest since it contains all the thermodynamic information needed such as the free energy F and the free energy density f. We consider a canonical ensemble without chemical potentials: A system of constant volume $\mathcal{V}$ in contact with a heat reservoir[6] of temperature T. The corresponding free energy and free energy density read

$$F(T, \mathcal{V}, N) = \frac{1}{\beta} \ln \mathcal{Z}(T, \mathcal{V}) = T \ln \mathcal{Z}(T, \mathcal{V}) \,, \tag{2.39}$$

$$f(T, \mathcal{V}, N) = \frac{1}{\beta \mathcal{V}} \ln \mathcal{Z}(T, \mathcal{V}) = \frac{T}{\mathcal{V}} \ln \mathcal{Z}(T, \mathcal{V}) \,, \tag{2.40}$$

where $\beta = T^{-1}$. We notice that, in the context of **thermal quantum field theory** (TQFT), the temperature has the unit of energy. Energy E and entropy S can be derived from the free energy via Legendre transformation as

$$F(T, \mathcal{V}, N) = E(T, \mathcal{V}, N) - TS(T, \mathcal{V}, N) \,. \tag{2.41}$$

The partition function is:

$$\mathcal{Z}(T) = \mathrm{Tr}\big[\, \mathrm{e}^{-\beta H}\,\big] \,, \tag{2.42}$$

where H denotes the Hamiltonian and the trace spans the entire Hilbert space. After performing a Wick rotation $\tau \equiv it$ and setting $\tau = T^{-1}$, the operator $\mathrm{e}^{-\beta H}$ in Eq. (2.42) equals the time evolution operator e^{-iHt} in classical quantum mechanics. The path-integral representation in imaginary-time formalism [12] of the partition function is given by:

$$\mathcal{Z} = \int_{\phi(\beta,x)=\phi(0,x)} \mathcal{D}\phi(\tau,x) \, \exp\left\{ -\underbrace{\int_0^\beta d\tau \int d^3x \, \mathcal{L}_E(\phi, \partial\phi)}_{S_E} \right\}, \tag{2.43}$$

where we integrate over all possible configurations of the field ϕ and introduce the Euclidian Lagrangian density $\mathcal{L}_E(\phi, \partial\phi)$ as well as the Euclidean action S_E.

We consider ϕ to be a real scalar field and express it as a sum of its zero- and non-zero-momentum modes (denoted as $\bar{\phi}$ and ϕ', respectively) [33]. The zero-momentum mode represents the lowest energy and consequently a minimum of the potential V.

The partition function then reads [33]

$$\mathcal{Z} = \int_{-\infty}^{+\infty} d\bar{\phi} \int_{P \neq 0} \mathcal{D}\phi' \, \exp\left(S_E(\phi = \bar{\phi} + \phi') \right) \tag{2.44}$$

---

[6]The thermal bath of the universe, in our research.

$$\equiv \int_{-\infty}^{+\infty} d\bar{\phi} \, \exp\left[-\frac{\mathcal{V}}{T} V_{\text{eff}}(\bar{\phi}, T)\right] , \tag{2.45}$$

where we first encounter the **thermal effective potential** V_{eff}. It includes in addition to the classical potential (now referred to as tree-level potential V_{tree}) also quantum corrections at zero temperature and thermal corrections at finite temperatures[7]. We perform a Taylor expansion of V_{eff} around its minimum $\bar{\phi}_{\text{min}}$:

$$V_{\text{eff}}(\bar{\phi}, T) \approx V_{\text{eff}}(\bar{\phi}_{\text{min}}, T) + \frac{1}{2} V_{\text{eff}}''(\bar{\phi}_{\text{min}}, T)(\bar{\phi} - \bar{\phi}_{\text{min}})^2 . \tag{2.46}$$

Inserting Eq. (2.46) in Eq. (2.45), we obtain the following integral:

$$\mathcal{Z}(T, \mathcal{V}) \approx \int_{-\infty}^{+\infty} d\bar{\phi} \, \exp\left[-\frac{\mathcal{V}}{T} V_{\text{eff}}(\bar{\phi}_{\text{min}}, T)\right] \exp\left[\frac{1}{2} V_{\text{eff}}''(\bar{\phi}_{\text{min}}, T)(\bar{\phi} - \bar{\phi}_{\text{min}})^2\right] . \tag{2.47}$$

The first term can be pulled in front of the integral. We integrate the Gaussian and obtain the following solution:

$$\mathcal{Z}(T, \mathcal{V}) \approx \sqrt{\frac{2\pi T}{V_{\text{eff}}''(\bar{\phi}_{\text{min}}, T)\mathcal{V}}} \exp\left[-\frac{\mathcal{V}}{T} V_{\text{eff}}(\bar{\phi}_{\text{min}}, T)\right] . \tag{2.48}$$

In the thermodynamic limit $\mathcal{V} \to \infty$, Eq. (2.40) yields the following relationship between free energy density f and thermal effective potential [33]:

$$\lim_{V \to \infty} f(T) = V_{\text{eff}}(\bar{\phi}_{\text{min}}, T) + \mathcal{O}\left(\frac{\ln \mathcal{V}}{\mathcal{V}}\right) . \tag{2.49}$$

We make the following conclusion: In the thermodynamic limit, the free energy density is represented by the minimum of the thermal effective potential. Since a FOPT is characterized by a discontinuity in $\frac{df(T)}{dT}|_{T=T_c}$ at a critical temperature T_c, the same behaviour is expected from $V_{\text{eff}}(\bar{\phi}_{\text{min}}, T_c)$. In that case, the discontinuity results from the emergence of a second minimum separated from the first one by a thermal barrier (see Fig. 2.5). One refers to the second minimum as **vacuum expectation value** (VEV) $\langle\phi\rangle \neq 0$ of the scalar field.

2.2.2 Bubble nucleation

We already introduced the false vacuum as the metastable phase of the universe before undergoing a PT. Usually, when the scalar tunnels to the true vacuum one speaks of **false vacuum decay** (see Calan and Coleman [8][9] for zero temperature and Linde [34] for finite temperatures). Let us consider the temperature-dependent nucleation rate per unit volume for bubbles of true vacuum [34]:

$$\frac{\Gamma(T)}{\mathcal{V}} \simeq T^4 \left(\frac{S_3}{2\pi T}\right)^{3/2} \mathrm{e}^{-S_3/T} , \tag{2.50}$$

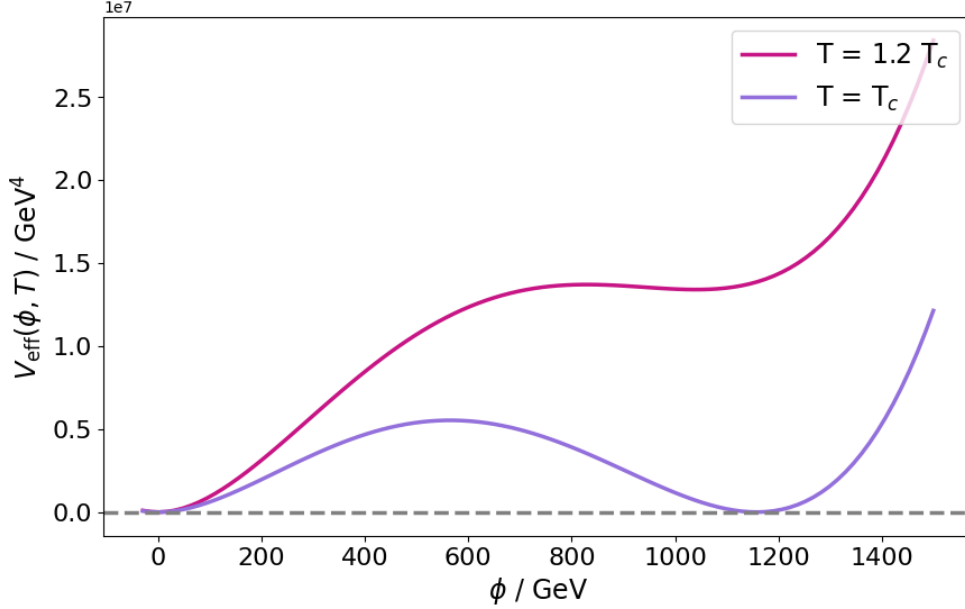[7]Details on the construction of V_{eff} can be found in [6].

Fig. 2.5: Temperature evolution of an exemplary thermal effective potential in the Abelian Higgs model (cf. Eq. 3.12 – 3.17). At critical temperature T_c, a thermal barrier separates two degenerate generate minima representing two distinct, coexisting phases.

where the four-dimensional Euclidean action S_4 (an integral over $\beta = T^{-1}$ for O(4)-symmetric bubbles at zero temperature) has now simplified to $S_4 = \frac{S_3}{T}$. Note that in the considered case, the false vacuum decays due to thermal fluctuations. The three-dimensional Euclidean action is

$$S_3 = \int d^3x \left[\frac{1}{2} (\nabla \phi)^2 + \left(V_{\text{eff}}(\phi, T) - V_{\text{eff}}(0, T) \right) \right], \tag{2.51}$$

and leads to the following equation of motion [34]:

$$\frac{d^2\phi}{dr^2} + \frac{2}{r} \frac{d\phi}{dr} = \frac{dV_{\text{eff}}}{d\phi}, \tag{2.52}$$

where $r = \sqrt{x^2 + t^2}$ is the three-dimensional bubble radius that grows with time t. We refer to Eq. (2.52) as the O(3)-symmetric bounce equation.

The bounce solution can be obtained with the following boundary conditions:

$$\phi \to 0 \qquad \text{at} \qquad r \to \infty, \tag{2.53a}$$

$$\frac{d\phi}{dr} = 0 \qquad \text{at} \qquad r = 0. \tag{2.53b}$$

For a method to numerically determine the bounce solution, see chapter 4. A plot of the bubble wall profile for various temperatures can be found in Fig. 2.6.
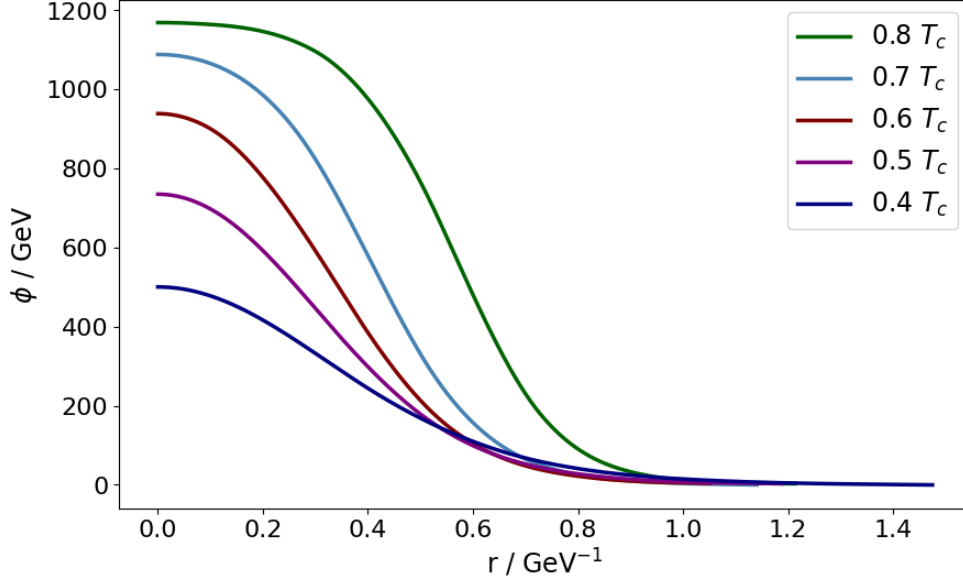
Fig. 2.6: Bubble wall profile for various temperatures in the Abelian Higgs model. The bubble wall expands for decreasing temperatures.

The probability that the false vacuum has not yet decayed into true vacuum at a given point is determined by $P = e^{-I(T)}$, where [16]

$$I(T) = \frac{4\pi}{3} \int_T^{T_c} \frac{dT'\Gamma(T')}{T'^4 H(T')} \left(\int_T^{T'} \frac{d\tilde{T}}{H(\tilde{T})} \right)^3 , \qquad (2.54)$$

with the Hubble parameter [16]

$$H^2 = \frac{\rho_{\text{vac}} + \rho_{\text{rad}}}{3M_{\text{pl}}^2} = \frac{1}{3M_{\text{pl}}^2} \left(\Delta V + \frac{\pi^2}{30} g_* T^4 \right) . \qquad (2.55)$$

We notice that $H(T)$ is proportional to the vacuum energy density $\rho_{\text{vac}} \equiv \Delta V = V_{\text{eff}}(0, T) - V_{\text{eff}}(\phi_{\text{true}}, T)$ and the radiation energy density $\rho_{\text{rad}} \equiv \frac{\pi^2}{30} g_* T^4$. Furthermore, the effective number of relativistic dofs g_* is introduced. In the following, we assume $g_* = 100$ for simplicity.[8]

2.2.3 Bubble collisions

At critical temperature T_c, stable and metastable phase coexist, allowing thermal tunneling to happen. The PT, however, only takes place when bubbles of true vacuum form fast enough to overcome the expansion of the universe. This is possible for $\Gamma(T = T_n)/H^4(T = T_n) \sim 1$ at nucleation temperature T_n. The expansion is then

---

[8]Note that in the SM this value is $g_* = 106.75$.

driven by an effective pressure due to the potential difference between true and false vacuum.

When solving Eq. (2.54) for $I(T) = 0.34$ [15], we obtain the percolation temperature $T = T_*$ of the PT. There are many important quantities that can be evaluated at T_* such as the PT strength α, the average bubble radius R_* at percolation or the inverse PT duration β. These quantities will help us to understand the further bubble dynamics up until their collision and the corresponding generation of GWs.

The PT strength α is a measure of how much latent heat is released during the phase transition. It reflects the amount of released energy that will go into the expansion of true vacuum bubbles and how much thermal energy will go into the reheating of the symmetric phase.[9] Therefore, it reads [21]:

$$\alpha = \frac{\rho_{\mathrm{vac}}(T_*)}{\rho_{\mathrm{rad}}(T_*)} = \frac{\Delta V}{\pi^2 g_* T_*^4/30} \ . \tag{2.56}$$

The average bubble radius at percolation R_* is [16]:

$$R_* = \left[T_* \int_{T_*}^{T_c} \frac{dT'\Gamma(T')}{T'^2 H(T')} \mathrm{e}^{-I(T')} \right]^{-\frac{1}{3}} \ . \tag{2.57}$$

It can be used to calculate the inverse PT duration [16]:

$$\beta = \frac{\left(8\pi\right)^{\frac{1}{3}}}{R_*} \ . \tag{2.58}$$

What is often done in the literature is to normalize Eq. (2.58) to the Hubble parameter. Then, $\frac{\beta}{H}$ provides information on the inverse duration of the PT with respect to the expansion rate of the universe. For larger $\frac{\beta}{H}$, the PT proceeds more slowly and more bubbles of true vacuum can nucleate and collide.

2.2.4   Gravitational waves from bubble collisions

We are interested in GWs generated as a consequence of cosmological FOPTs and the corresponding collision of true vacuum bubbles. We will therefore compute the stochastic GW spectrum $h^2\Omega_{\mathrm{GW}}$ with its various contributions to the observable SGWB. The following mechanisms generate GWs and add to the spectrum:

1. **Collisions of vacuum bubbles** $h^2\Omega_\phi$

2. **Propagation of sound waves** in the thermal bath of the primordial plasma $h^2\Omega_{\mathrm{sw}}$

3. **Magnetohydrodynamic (MHD) turbulences** $h^2\Omega_{\mathrm{turb}}$.

---

[9]Concretely, reheating happens for the thermal bath of the false vacuum where $\langle\phi\rangle = 0$.
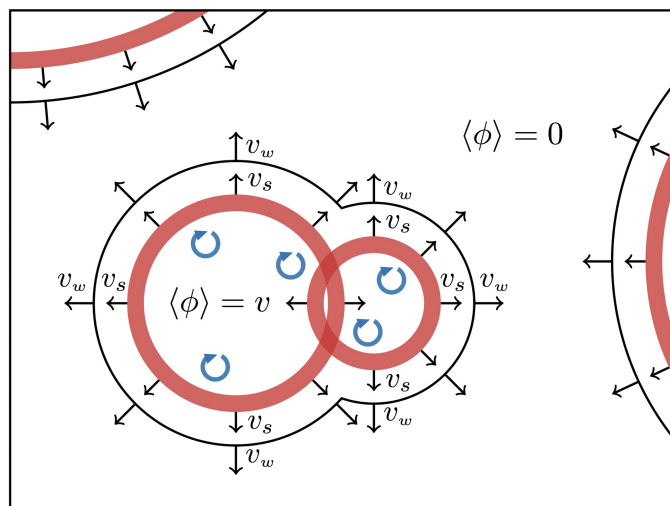
Fig. 2.7: A simplified scheme of the GW generation from bubble collision (black), sound waves in the plasma (red), and turbulences (blue). Figure adopted from [39]

The collision of bubbles results in anisotropies in the energy momentum tensor and GWs are generated as a result of a quadrupole moment that changes with time (cf. Sec. 2.1.2) . This contribution to the GW spectrum depends exclusively on the scalar field's dynamics (hence the index ϕ). We will use the envelope approximation [32] assuming that most of the energy is deposited in a thin shell surrounding the walls of uncollided bubbles. We therefore set $h^2\Omega_\phi \equiv h^2\Omega_{\text{env}}$ [21].

The bubble collisions create sound waves in the primordial plasma which for their part shape into sound bubbles that eventually collide and generate GWs. Furthermore, they represent a longer-lasting source of GWs in comparison to the initial bubble wall collisions and contribution to the GW spectrum are amplified by a factor $\frac{\beta}{H}$ [6]. Consequently, sound wave collisions typically dominate the GW spectrum.

Another result of sound wave propagation is the induction of vortical motions in the ionized primordial plasma [39]. These MHD turbulences also produce GWs. However, we will neglect the conversion into turbulent motion since it affects only a fraction of the sound wave energy budget [7].

The GW spectrum is the sum of its contributions:

$$h^2\Omega_{\text{GW}} \simeq h^2\Omega_{\text{env}} + h^2\Omega_{\text{sw}} \ . \tag{2.59}$$

An important ingredient for the computation of $h^2\Omega_{\text{GW}}$ are the efficiency factors κ_v for the amount of latent heat converted into bulk motion and κ_ϕ for the energy fraction that goes into the bubble wall acceleration [21]:

$$\kappa_v \simeq \alpha\big(0.73 + 0.083\sqrt{\alpha} + \alpha\big)^{-1} \quad (v_w \sim 1)\,, \tag{2.60}$$

$$\kappa_\phi \equiv \frac{\alpha - \alpha_\infty}{\alpha}\,, \tag{2.61}$$

with the model-dependent parameter α_∞. It can be calculated via [21]:

$$\alpha_\infty \simeq \frac{30}{24\pi^2} \frac{\sum_a n_a \Delta m_a^2(\phi)}{g_* T_*^2} \,, \tag{2.62}$$

where n_a denotes the dof of particle species a and $\Delta m_a^2(\phi)$ incorporates all particle masses that change during the PT.

Finally, we are able to compute the GW spectrum. The contribution from bubble collisions in the envelope approximation is [21]:

$$h^2\Omega_{\text{env}}(f) = 1.67 \times 10^{-5} \left(\frac{H(T_*)}{\beta}\right)^2 \left(\frac{\kappa_\phi \alpha}{1+\alpha}\right)^2 \left(\frac{100}{g_*}\right)^{\frac{1}{3}} \left(\frac{0.11 v_w^3}{0.42 + v_w^2}\right) S_{\text{env}}(f) \,, \tag{2.63}$$

with frequency f and spectral shape $S_{\text{env}}(f)$ of the GW signal. The latter is given by

$$S_{\text{env}}(f) = \frac{3.8(f/f_{\text{env}})^{2.8}}{1 + 2.8(f/f_{\text{env}})^{3.8}} \,. \tag{2.64}$$

The corresponding peak frequency f_{env} depends on the inverse PT duration β. At percolation, it is [21]:

$$f_* = \beta \left(\frac{0.62}{1.8 - 0.1 v_w + v_w^2}\right) \,. \tag{2.65}$$

Red-shifted, the peak frequency develops to [21]

$$f_{\text{env}} = 16.5 \times 10^{-3}\text{mHz} \left(\frac{f_*}{\beta}\right) \left(\frac{\beta}{H(T_*)}\right) \left(\frac{T_*}{100\text{GeV}}\right) \left(\frac{g_*}{100}\right)^{\frac{1}{6}} \,, \tag{2.66}$$

considering a radiation-dominated era after the FOPT and a subsequent adiabatic expansion of the universe until today.

The GW signal resulting from the sound wave contribution reads [21]

$$h^2\Omega_{\text{sw}}(f) = 2.65 \times 10^{-6} \left(\frac{H(T_*)}{\beta}\right) \left(\frac{\kappa_v \alpha}{1+\alpha}\right)^2 \left(\frac{100}{g_*}\right)^{\frac{1}{3}} v_w S_{\text{sw}}(f) \,, \tag{2.67}$$

with the spectral shape

$$S_{\text{sw}}(f) = (f/f_{\text{sw}})^3 \left(\frac{7}{4 + 3(f/f_{\text{sw}})^2}\right)^{\frac{7}{2}} \,. \tag{2.68}$$

We adopt the peak frequency in [21] $f'_{\text{sw}} = (2/\sqrt{3})(\beta/v_w)$ which reads after red-shifting:

$$f_{\text{sw}} = 1.9 \times 10^{-2}\text{mHz} \, \frac{1}{v_w} \left(\frac{\beta}{H(T_*)}\right) \left(\frac{T_*}{100\text{GeV}}\right) \left(\frac{g_*}{100}\right)^{\frac{1}{6}} \,. \tag{2.69}$$

2.2.5 Computation of the power-law integrated sensitivity curves

We will check whether the computed GW spectrum overlaps the enclosed regions by the **power-law integrated** (PLI) sensitivity curves [43] of the considered planned space-based interferometers.[10] If a GW spectrum has a large enough **signal-to-noise ratio** (SNR), it will intersect the enclosed region and consequently be detected. We obtain the PLI sensitivity curve using the SNR via the following steps:

The SNR ρ is given by [7]

$$\rho^2 = 2t_{\mathrm{obs}} \int_{f_{\mathrm{min}}}^{f_{\mathrm{max}}} df \left[\frac{h^2 \Omega_{\mathrm{GW}}(f)}{h^2 \Omega_{\mathrm{eff}}(f)} \right]^2 , \tag{2.70}$$

with the observation time t_{obs}, the detector frequency band $(f_{\mathrm{min}}, f_{\mathrm{max}})$ and the effective noise energy density $h^2 \Omega_{\mathrm{eff}}$. One can assume the following power law:

$$h^2 \Omega_{\mathrm{GW}}(f) = h^2 \Omega_b \left(\frac{f}{\bar{f}} \right)^b , \tag{2.71}$$

where b is the spectral index and $h^2 \Omega_b$ the GW density at a reference frequency $\bar{f}$. The power law signal can be detected if $h^2 \Omega_b$ is larger than at a certain threshold value ρ_{thr}:

$$h^2 \Omega_b > h^2 \Omega_b^{\mathrm{thr}}(f) \equiv \frac{\rho_{\mathrm{thr}}}{\sqrt{2t_{\mathrm{obs}}}} \left[\int_{\mathrm{min}}^{f_{\mathrm{max}}} df \left(\frac{(f/\bar{f})^b}{h^2 \Omega_{\mathrm{eff}}(f)} \right)^2 \right]^{-\frac{1}{2}} . \tag{2.72}$$

The PLI sensitivity curve is then given as follows [7]:

$$h^2 \Omega_{\mathrm{PLI}}(f) = \max_b \left[h^2 \Omega_b^{\mathrm{thr}} \left(\frac{f}{\bar{f}} \right)^b \right] . \tag{2.73}$$

---

[10]All PLI curves in this thesis were provided by Daniel Schmitt.

2.3 The Higgs mechanism

In the 1960s, six physicists published their theory on the unknown origin of particle masses: François Englert, Robert Brout [17], Peter Higgs [29], Gerald Guralnik, Carl R. Hagen and Tom Kibble [28]. The **Higgs mechanism** was born. Its concept is the spontaneous breaking of a given symmetry as the Higgs field (a complex doublet with hypercharge $Y = \frac{1}{2}$, referred to as the **Higgs multiplet**) acquires a VEV. The corresponding Higgs boson was discovered at CERN in 2012 [22] which finally confirmed the Higgs field's existence predicted by the theory.

In the context of Sheldon L. Glashow's electroweak unified theory [26], Steven Weinberg [45] and Abdus Salam [41] applied in 1967 the Higgs mechanism to the electroweak symmetry resulting in a spontaneous breakdown into electromagnetism[11]:

$$SU(2)_L \times U(1)_Y \longrightarrow U(1)_{EM}, \tag{2.74}$$

where $SU(2)_L$ denotes the weak isospin and $U(1)_Y$ the weak hypercharge symmetry group. The $W^\pm$ and Z boson obtain their masses through the Higgs mechanism. However, instead of explaining the details of the Higgs mechanism in the electroweak theory, we will illustrate it in the next chapter on the simpler Abelian Higgs model.

---

[11]This will later lead to the Glashow-Weinberg-Salam (GWS) Standard Model of particle physics.

CHAPTER 3
THE MODEL

We consider an Abelian, $U(1)$-gauge extension of the Standard Model: The Abelian Higgs model. The following introduction is inspired by Kien Nguyens [38] and Laura Reinas [40] lecture notes. Afterwards, I will derive the thermal effective potential, following [6]

At this point, it should be noted that we initially dealt with the model of a real, massive scalar field that only couples to itself. After we found that such a model has no FOPT, we moved on to the Abelian Higgs model. Details on the first model can be found in Appendix A but are not focus of this thesis.

3.1 The Abelian Higgs model

Let us first consider the $U(1)$ gauge invariant kinetic term of the photon

$$\mathcal{L}_{\text{kin}} = -\frac{1}{4} F_{\mu\nu} F^{\mu\nu} \,, \tag{3.1}$$

with the electromagnetic tensor

$$F_{\mu\nu} = \partial_\mu A_\nu - \partial_\nu A_\mu \,. \tag{3.2}$$

Suppose we want to have a theory that describes a massive photon and therefore simply add a mass term m^2:

$$\mathcal{L}_{\text{kin}} = -\frac{1}{4} F_{\mu\nu} F^{\mu\nu} + \frac{1}{2} m^2 A_\mu A^\mu \,. \tag{3.3}$$

However, the mass term violates the local $U(1)$ gauge symmetry, meaning that the Lagrangian density is no longer invariant under the transformation

$$A_\mu(x) \to A_\mu(x) - \partial_\mu \eta(x) \,, \tag{3.4}$$

for any η and x. There is still a way we can extend the model to provide us with a massive photon: We introduce a charged, self-coupling complex scalar field that also couples to the vector field A_μ. The new Lagrangian density reads in Minkowskian metric [38]

$$\mathcal{L} = -\frac{1}{4} F_{\mu\nu} F^{\mu\nu} + (D_\mu \phi)^\dagger (D^\mu \phi) - V(\phi) \,, \tag{3.5}$$

with the gauge covariant derivative $D_\mu = \partial_\mu - igA_\mu$ (where g denotes the charge of the vector field) and the following potential:

$$V(\phi) = -\frac{\mu^2}{2}\phi^\dagger\phi + \frac{\lambda}{4}(\phi^\dagger\phi)^2 \ . \tag{3.6}$$

The new Lagrangian density is invariant under Eq. (3.4) and under

$$\phi(x) \to e^{iq\eta(x)}\phi(x) \ . \tag{3.7}$$

The parameter μ^2 of the potential $V(\phi)$ is now of special interest for us since its sign is crucial for which theory we describe: That of a massless or a massive photon. For $\mu^2 < 0$, the potential has one global minimum at $\phi = 0$. The photon remains massless. In that case, the theory describes quantum electrodynamics (QED) with a massive scalar field. For $\mu^2 > 0$, we observe the appearance of two degenerate minima

$$\langle\phi\rangle = \pm\sqrt{\frac{\mu^2}{\lambda}} \ , \tag{3.8}$$

leaving us with a Mexican hat potential. After choosing one ground state, the $U(1)$ symmetry is spontaneously broken.

Next, we want to express the Lagrangian density in a form that appears more intuitive to us. For that, we choose the following parametrization for our complex scalar field ϕ:

$$\phi = \frac{v + h}{\sqrt{2}}e^{i\frac{\chi}{v}} \ , \tag{3.9}$$

where $v = \sqrt{\frac{\mu^2}{\lambda}}$ is our VEV, h denotes the Higgs boson and χ the Goldstone boson. Both bosons are real scalar fields. The Goldstone boson, however, is massless. We use our parametrization in Eq. (3.9) and end up with the new Lagrangian density [40]

$$\mathcal{L} = \underbrace{-\frac{1}{4}F_{\mu\nu}F^{\mu\nu} + \frac{g^2v^2}{2}A_\mu A^\mu}_{\text{massive vector field}} + \underbrace{\frac{1}{2}(\partial_\mu h \ \partial^\mu h - 2\mu^2 h^2)}_{\text{massive real scalar field}} + \underbrace{\frac{1}{2}\partial_\mu\chi \ \partial^\mu\chi - gvA_\mu\partial^\mu\chi}_{\text{massless Goldstone Boson}} \ . \tag{3.10}$$

Applying the unitary gauge $A_\mu \to A'_\mu = A_\mu - \frac{1}{gv}\partial_\mu\chi$ will make the Goldstone boson disappear:

$$\mathcal{L} = \underbrace{-\frac{1}{4}F_{\mu\nu}F^{\mu\nu} + \frac{g^2v^2}{2}A'_\mu A'^\mu}_{\text{massive vector field}} + \underbrace{\frac{1}{2}(\partial_\mu h \ \partial^\mu h - 2\mu^2 h^2)}_{\text{massive real scalar field}} \ . \tag{3.11}$$

Now our theory describes a dark photon with effective mass $m_Z = gv$ and a Higgs boson with mass $m_h = \sqrt{2}\mu = \sqrt{2\lambda}v$. The **degrees of freedom** (dof) before and after **spontaneous symmetry breaking** (SBB) are equal. Initially, we have 4 dof: 2 dof from the massless photon and 2 dof from the complex scalar field. In the end, we have a massive photon with 3 dof and a real scalar field with 1 dof, leaving us

particle a	effective mass $m_a(\phi)$	dof	C_a	thermal mass $\Pi(\phi)$
ϕ	$-\mu^2 + 3\lambda\phi^2$	1	3/2	$\lambda T^2/4$
Z	$g^2\phi^2$	3	5/6	$g^2T^2/4$

Tab. 3.1: Thermal and effective masses of the respecitve particle inclduing their degrees of freedom along with their respective constants appearing in the thermal effective potential (Eq. 3.12 – 3.17)

again with 4 dof. Hence, one says: In unitary gauge, the Goldstone boson gets eaten by the gauge boson through the Higgs mechanism.

In Sec. 2.2.1 we established that, for $\mathcal{V} \to \infty$, the thermal effective potential $V_{\text{eff}}(\phi, T)$ resembles the free energy density $f(T)$. In the Abelian Higgs model, the individual contributions are [6]

$$V_{\text{eff}}(\phi, T) \approx V_{\text{tree}}(\phi) + V_{\text{CW}}(\phi, T = 0) + V_{\text{T}}(\phi, T) + V_{\text{daisy}}(\phi, T) \,, \tag{3.12}$$

with the temperature independent tree-level potential $V_{\text{tree}}(\phi)$ introduced in Eq. (3.6) and the zero-temperature Coleman-Weinberg potential [6]

$$V_{\text{CW}}(\phi, T = 0) = \sum_a \eta_a n_a \frac{m_a^4(\phi)}{64\pi^2} \Big[\log\Big(\frac{m_a^2(\phi)}{\Lambda^2}\Big) - C_a\Big] \,, \tag{3.13}$$

where we sum over the different particle types $a \in \{\phi, Z\}$. The parameter η is 1 (-1) for bosons (fermions). We encounter more new parameters: The field-dependent mass $m_a(\phi)$, the renormalization scale Λ for which we take the (positive) tree-level VEV in Eq. (3.9), the particles dof n_a and the particle dependent constant C_a. The values for our model are listed in Tab. 3.1.

The temperature-dependent contribution to the effective potential is [6]

$$V_{\text{T}}(\phi, T) = \frac{T^4}{2\pi^2} \sum_a \eta_a n_a J_{b/f}\Big(\frac{m_a^2(\phi)}{T^2}\Big) \,, \tag{3.14}$$

with the thermal function [11]

$$J_{b/f}(x^2) \equiv \int_0^\infty dy \, y^2 \log\big\{1 \mp \exp\big[-\sqrt{y^2 + x^2}\big]\big\} \,, \tag{3.15}$$

where $x \equiv \frac{m_a(\phi)}{T}$. For a better unterstanding of the thermal evolution, we expand the above integral in the high-temperature limit ($x \to 0$). As our model contains no fermions, we will only mention the expansion for bosons: [11]

$$J_b(x^2) \stackrel{x\to 0}{\approx} -\frac{\pi^4}{45} + \frac{\pi^2}{12}x^2 - \frac{\pi}{6}x^3 + \dots \,. \tag{3.16}$$

We notice a positive quadratic term, meaning that at high temperatures a parabolic shape with just one minimum at $\phi = 0$ is to be expected. The negative cubic term enables the occurrence of a thermal barrier at decreasing temperatures.

At high temperatures $(T \gg \mu)$ [11], thermal mass corrections $\Pi(T)$ have to be taken into account in order to restore the symmetry that is broken at T_c [2]. They are added to the effective mass in the daisy potential [6]

$$V_{\text{daisy}}(\phi, T) = -\frac{T}{12\pi} \sum_a \left[\left(m_a^2(\phi) + \Pi(T) \right)^{3/2} - \left(m_a^2(\phi) \right)^{3/2} \right] . \qquad (3.17)$$
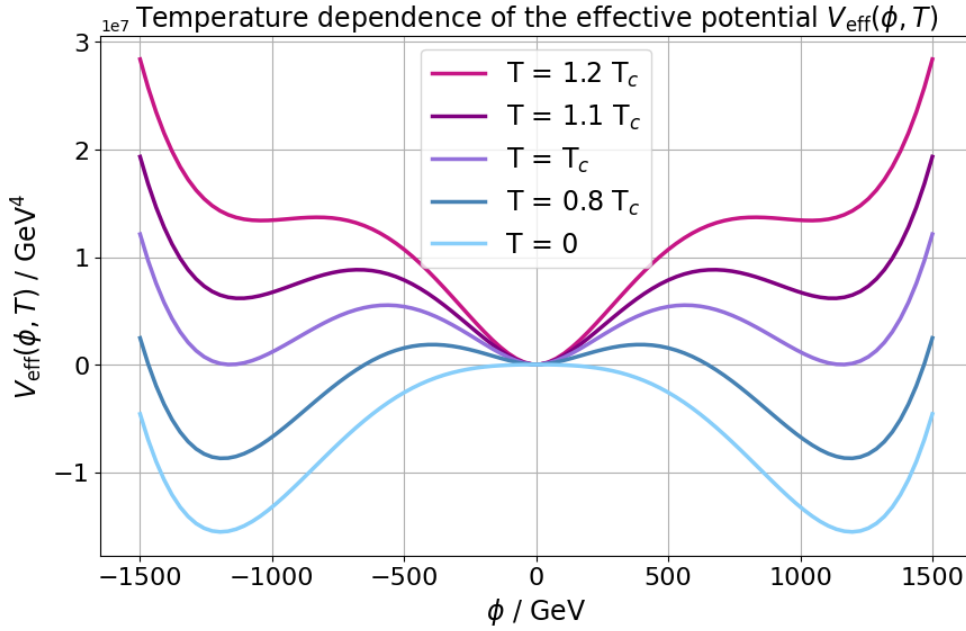

Fig. 3.1: Thermal effective potential $V_{\text{eff}}(\phi, T)$ (see Eq. 3.12 – 3.17) with m $= \sqrt{10}$ GeV, $g = 0.8$ and $\lambda = 10^{-9}$.

Now we have all our ingredients for the thermal effective potential (up to one-loop correction). From Fig. 3.1, we draw the following conclusions: In the hot early universe the field settles in the minimum at $\phi = 0$ and all symmetries are preserved. As temperatures drop, the symmetry-breaking minimum appears at $\phi \neq 0$. It is separated from the old minimum by a thermal barrier. As the Universe continues to cool down, the thermal barrier decreases until, at a critical temperature T_c, the minima are degenerate. Now both states are equally likely. At lower temperatures, the second minimum deepens, becoming energetically preferred and triggering a first order phase transition as the field tunnels into the deeper minimum. Finally, at zero temperature, $\phi = 0$ becomes the local maximum.

CHAPTER 4
NUMERICAL IMPLEMENTATION

For all numerical calculations, we used the language `Python`. Besides its standard packages for scientific applications and visualization of data, like `scipy`, `numpy` and `matplotlib`, we used the toolkit `CosmoTransitions`[1] [44], which was specifically designed for analyzing cosmological PTs in the framework of this thesis, i.e. when considering a scalar field that is under the influence of an effective potential at some finite temperature. All notebooks created while working on this thesis can be found here: `https://github.com/DMGW-Goethe/Rebeccas-BA/tree/master`

4.1 Solving the bounce equation

As mentioned in Sec. 2.2.2, we have to find solutions to a particular second-order differential equation to find the critical bubble profile that minimizes the three-dimensional Euclidean action S_3. We have (cf. Eq. 2.52)

$$\frac{d^2\phi}{dr^2} = \frac{dV_{\text{eff}}(\phi,T)}{d\phi} - \frac{2}{r}\frac{d\phi}{dr}\,, \tag{4.1a}$$

$$\frac{d\phi}{dr}\bigg|_{r=0} = 0, \quad \lim_{|r|\to\infty}\phi(r) = 0\,, \tag{4.1b}$$

where Eq. (4.1a) is the so-called **bounce equation**. To solve this **boundary-value problem** (BVP), we follow the analogy given by Coleman in [9] and notice that Eq. (4.1a) can be identified with the equation of motion of a particle ϕ, which moves with time r in a potential $-V_{\text{eff}}$ and a damping force proportional to $\frac{1}{r}$. With this observation, we can transform the BVP into an **initial-value problem** (IVP): The unknown initial value $\phi(0) = \phi_0$, which is expected to be close to the true vacuum, has to be chosen so that $\phi(r)$ is strictly decreasing and asymptotically approaching 0 at the local maximum of the inverted effective potential $-V_{\text{eff}}$. An effective way to solve this IVP is the **shooting method**: If ϕ_0 is chosen too high, then it *overshoots* the correct solution which means that it reaches 0 after some finite time and proceeds to move further away, approaching the negative thermal barrier ϕ_-. Similarly, if ϕ_0 is chosen to low, then it *undershoots* the solution, never reaching 0 and approaching the positive thermal barrier ϕ_+. Now, for every guess of ϕ_0, we can numerically solve

---

[1] `https://github.com/clwainwright/CosmoTransitions`

the system of differential equations

$$y_1' = y_2 \, , \qquad\qquad y_1(0) = \phi_0, \tag{4.2a}$$

$$y_2' = \frac{dV_{\text{eff}}}{d\phi} - \frac{2}{r}y_2 \, , \quad y_2(0) = 0, \tag{4.2b}$$

with $y_1(r) := \phi(r)$ and $y_2(r) := \frac{d\phi(r)}{dr}$, e.g. using the Finite Difference method or, in practice, a function like `scipy.integrate.solve_ivp`, where we choose the interval of integration to be $[r = 0, r = R]$ with some large R. Based on how the solution behaves for different initial values, i.e. if $\phi(R; \phi_0)$ is moving further from or closer to 0 (also taking changes in sign into account), we can adjust the initial value ϕ_0 accordingly. This process is equivalent to numerically computing a root of $\phi(R; \phi_0)$ to some finite precision and can thus be automated by a root-finding algorithm such as the bisection method that can be aborted when the desired accuracy is achieved. However, since the second boundary condition in Eq. (4.1b) involves infinity and R cannot be made arbitrarily large without expecting performance issues, we can always only make initial guesses that either over- or undershoot the correct solution.

In this thesis, however, we use the above method as implemented in the `CosmoTransitions` class `SingleFieldInstanton` with the member function `findProfile` [1]. It should be noted at this point that Daniel Schmitt provided me with his code for finding the bubble profile and determining the bounce action.

CHAPTER 5

RESULTS

In the following, we present the GW spectra computed with Eqs. (2.63) and (2.67) and compare them with the power law integrated curves (shaded regions) of different planned space-based GW detectors along with the *gray violins* from Fig. 4 of the NANOGrav 15-year data set (*Search for Signals from New Physics*) [18] which correspond to the NANOGrav signal.[1] In doing so, we evaluate the GW spectra for different masses μ, gauge couplings g and self couplings λ of the Abelian Higgs model (see Eq. 3.11) and examine the corresponding dependence of the peak frequency f_{peak} and the peak amplitude $h^2 \Omega_{\mathrm{GW}}^{\mathrm{peak}}$.

Below, we always fix two parameters and vary the third one. The peak frequencies and peak amplitudes along with the values for the PT strength α and the inverse PT timescale $\frac{\beta}{H}$ are listed in tables associated with the respective GW spectrum.

Varying self couplings $\lambda \in \{10^{-17}, 10^{-9}, 10^{-7}\}$ for mass $\mu = \sqrt{7}$ GeV and gauge coupling $g = 0.3$.

Here, f_{peak} and $h^2 \Omega_{\mathrm{GW}}^{\mathrm{peak}}$ show a weak dependence on the self coupling λ (cf. Tab. 5.1). We observe lower peak frequencies with lower self coupling, but the magnitudes of f_{peak} only vary slightly. All peak frequencies lie in the frequency range of LISA and μAres (cf. Fig. 5.1).

The peak amplitudes increase for smaller self couplings. The GW signals cross the PLI curves of LISA, μAres, and BBO and therefore could be detected by each of them.

We notice that α remains roughly the same for all peak amplitudes and self couplings. Also, the PT proceeds much more slowly for larger self couplings.

λ	f_{peak}	$h^2 \Omega_{\mathrm{GW}}^{\mathrm{peak}}$	α	$\frac{\beta}{H}$
10^{-17}	$\sim \mathcal{O}(10^{-4}\ \mathrm{Hz})$	$\sim \mathcal{O}(10^{-7})$	~ 4	~ 20
10^{-9}	$\sim \mathcal{O}(10^{-3}\ \mathrm{Hz})$	$\sim \mathcal{O}(10^{-8})$	~ 4	~ 85
10^{-7}	$\sim \mathcal{O}(10^{-3}\ \mathrm{Hz})$	$\sim \mathcal{O}(10^{-8})$	~ 4	$\sim 9 \cdot 10^{20}$

Tab. 5.1: Values of f_{peak}, $h^2 \Omega_{\mathrm{GW}}^{\mathrm{peak}}$, α and $\frac{\beta}{H}$ for $\lambda \in \{10^{-17}, 10^{-9}, 10^{-7}\}$, $\mu = \sqrt{7}$ GeV and $g = 0.3$.

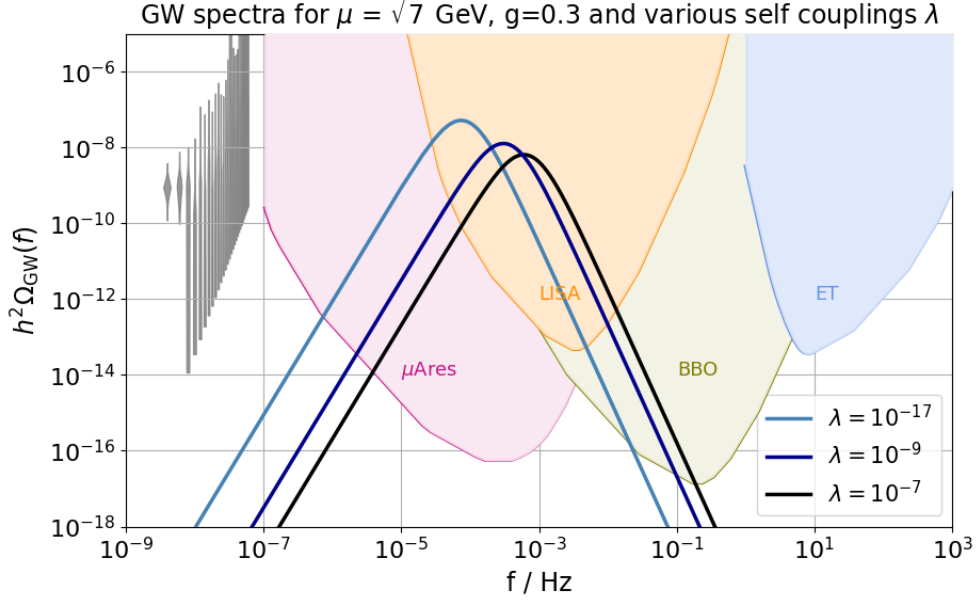[1]These violins were provided by Carlo Tasillo.

Fig. 5.1: GW spectra for various self couplings $\lambda \in \{10^{-17}, 10^{-9}, 10^{-7}\}$ for fixed mass $\mu = \sqrt{7}$ GeV and fixed gauge coupling $g = 0.3$.

Varying masses $\mu \in \{\sqrt{0.25}$ GeV$, \sqrt{2}$ GeV$, \sqrt{15}$ GeV$\}$ for gauge coupling $g = 0.8$ and self coupling $\lambda = 10^{-10}$.

We notice an increase of f_{peak} for bigger masses (cf. Tab. 5.2). All three peak frequencies fall within the frequency range of μAres, although for $\mu = \sqrt{0.25}$ GeV, it lies exactly at the limit (cf. Fig. 5.2).

A rise in the peak amplitude happens for smaller masses. The GW signals for $\mu \in \{\sqrt{0.25}$ GeV$, \sqrt{2}$ GeV$\}$ might be detectable with the NANOGrav signal as they intersect the gray violins. For $\mu = \sqrt{15}$ GeV, the peak amplitude is smaller. We can assume that the corresponding GW signal as well as the other two signals for smaller masses could be captured by μAres. In addition, the GW signal for $\mu = \sqrt{15}$ GeV crosses a small part of the LISA PLI curve therefore could possibly also be registered by LISA.

μ	f_{peak}	$h^2\Omega_{\text{GW}}^{\text{peak}}$	α	$\frac{\beta}{H}$
$\sqrt{0.25}$ GeV	$\sim \mathcal{O}(10^{-7}$ Hz$)$	$\sim \mathcal{O}(10^{-5})$	~ 6185	~ 0.3
$\sqrt{2}$ GeV	$\sim \mathcal{O}(10^{-6}$ Hz$)$	$\sim \mathcal{O}(10^{-6})$	~ 130	$\sim 4 \cdot 10^{20}$
$\sqrt{15}$ GeV	$\sim \mathcal{O}(10^{-5}$ Hz$)$	$\sim \mathcal{O}(10^{-7})$	~ 3	$\sim 8 \cdot 10^{20}$

Tab. 5.2: Values of f_{peak}, $h^2\Omega_{\text{GW}}^{\text{peak}}$, α and $\frac{\beta}{H}$ for $\mu \in \{\sqrt{0.25}$ GeV$, \sqrt{2}$ GeV$, \sqrt{15}$ GeV$\}$, $\lambda = 10^{-10}$ and $g = 0.8$
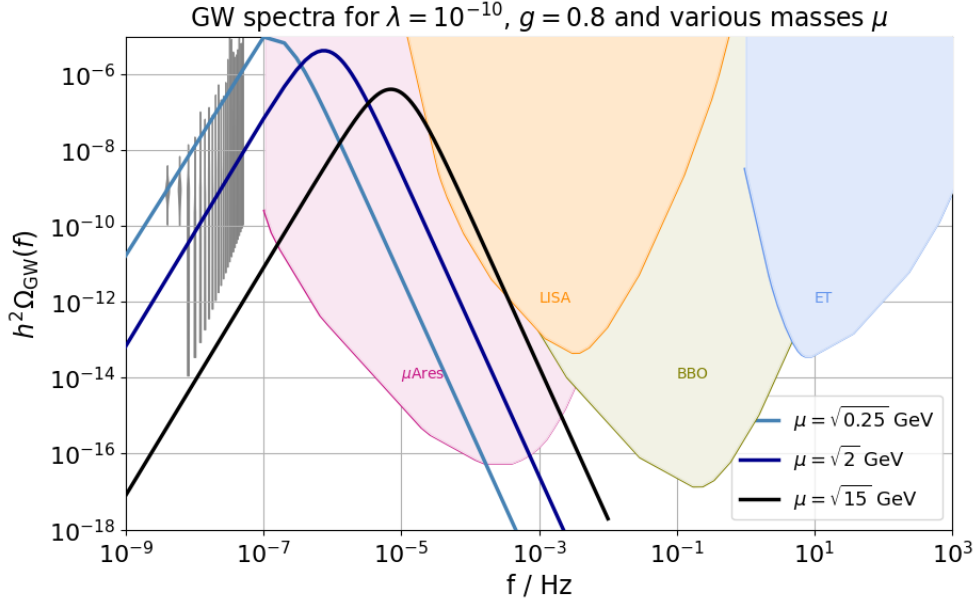
Fig. 5.2: GW spectra for various masses $\mu \in \{\sqrt{0.25}$ GeV$, \sqrt{2}$ GeV$, \sqrt{15}$ GeV$\}$, for fixed self coupling $\lambda = 10^{-10}$ and for gauge coupling $g = 0.8$.

The GW singal with the highest peak amplitude has the largest α. Hence: For decreasing masses, α becomes larger. Moreover, the slowest PT happens for the largest mass.

Varying gauge couplings $g \in \{0.3, 0.5, 0.8\}$ for mass $\mu = \sqrt{7}$ GeV and self coupling $\lambda = 10^{-10}$.

We notice a strong dependence on the gauge coupling in general (cf. Tab. 5.3). The peak frequencies increase with g. For $g = 0.3$, f_{peak} lies in the middle of the frequency range of LISA (cf. Fig. 5.3). For stronger gauge couplings $g \in \{0.5, 0.8\}$, the peak frequencies leave the range covered by LISA but still fall within the frequency range of μAres.

While the peak frequency increases for stronger gauge couplings, the peak amplitude decreases. The largest amplitudes are for gauge coupling $g \in \{0.5, 0.8\}$. Their GW signals intersect the PLI curve of μAres. The GW signal for $g = 0.5$ might also

g	f_{peak}	$h^2\Omega_{\text{GW}}^{\text{peak}}$	α	$\frac{\beta}{H}$
0.3	$\sim \mathcal{O}(10^{-3}$ Hz$)$	$\sim \mathcal{O}(10^{-8})$	~ 27	~ 448
0.5	$\sim \mathcal{O}(10^{-5}$ Hz$)$	$\sim \mathcal{O}(10^{-6})$	~ 131	$\sim 2 \cdot 10^{20}$
0.8	$\sim \mathcal{O}(10^{-6}$ Hz$)$	$\sim \mathcal{O}(10^{-6})$	~ 185	~ 0.6

Tab. 5.3: Values of f_{peak}, $h^2\Omega_{\text{GW}}^{\text{peak}}$, α and $\frac{\beta}{H}$ for $g \in \{0.3, 0.5, 0.9\}$, $\mu = \sqrt{7}$ GeV and $\lambda = 10^{-10}$.
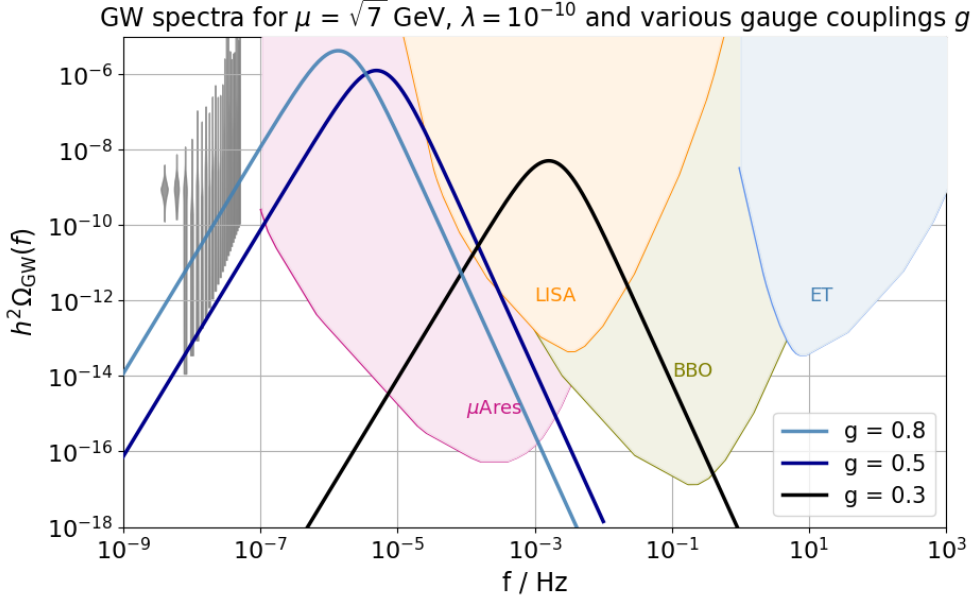
Fig. 5.3: GW spectra for various gauge couplings $g \in \{0.3, 0.5, 0.8\}$ for fixed mass $\mu = \sqrt{7}$ GeV and for fixed self coupling $\lambda = 10^{-10}$.

be detectable by LISA, since it overlaps with a small part of the PLI curve. Furthermore, the signal for $g = 0.8$ intersects the gray violins from NANOGrav and can thus presumably be registered with PTAs. The smallest amplitude is for $g = 0.3$. Still, the corresponding GW signal lies in the PLI curves of LISA, μAres and BBO and has good chances to be detected by at least one of them.

The GW signal with the highest peak amplitude also has the largest PT strength α (cf. Tab. 5.3). We notice a decrease of $h^2\Omega_{\mathrm{GW}}^{\mathrm{peak}}$ for smaller α. Furthermore, the smaller the gauge coupling, the smaller the PT strength. Additionally, for larger g, the PT proceeds more slowly. However, for $g = 8$ the inverse time scale is very small compared to the other values and does not correspond to the previous behavior. The unusual value for $\frac{\beta}{H}$ could result from the fact that large gauge coupling values are no longer perturbative.

We summarize our findings in the following:

1. An increase of the self coupling λ results in higher f_{peak} without a strong decrease of $h^2\Omega_{\mathrm{GW}}^{\mathrm{peak}}$ while α remains approximately the same. The PT proceeds more slowly for larger self couplings.

2. With smaller masses μ, f_{peak} drops while $h^2\Omega_{\mathrm{GW}}^{\mathrm{peak}}$ increases. For smaller masses, the corresponding PT strength is larger and the PT happens faster.

3. For smaller gauge couplings g, f_{peak} shifts to higher frequencies while $h^2\Omega_{\mathrm{GW}}^{\mathrm{peak}}$ decreases. Furthermore, smaller g result in weaker and faster PTs.

Finally, the following behavior from α and $\frac{\beta}{H}$ can be observed: Stronger PTs can be associated with larger peak amplitudes and lower peak frequencies in the GW spectrum (cf. Tabs. 5.1–5.3). More slowly proceeding PTs tend to smaller peak amplitudes and higher peak frequencies (cf. Tabs. 5.1–5.2).

CHAPTER 6
SUMMARY AND OUTLOOK

The aim of this thesis was to compute various GW spectra resulting from the aftermath of a FOPT in the Abelian Higgs model and to investigate whether these could potentially be detected by PTAs or future GW experiments. For this purpose, we have discussed the role of the thermal effective potential $V_{\text{eff}}(\phi, T)$ in a FOPT (see Sec. 2.2.1) and introduced the mechanism of the false vacuum decay with the involved bubble nucleation, bubble collision and sound wave propagation in Sec. 2.2.2 – 2.2.4.

A numerical analysis of the bounce solution was discussed in chapter 4, explaining the shooting method which is used in the member function `findProfile` of the `CosmoTransitions` class `SingleFieldInstanton` [1].

We constructed the thermal effective potential $V_{\text{eff}}(\phi, T)$ up to one-loop order in Sec. 3.1 and studied its temperature dependence. The scalar field ϕ is trapped in the symmetric phase at high temperatures in the early universe. For lower temperatures, a thermal barrier emerges and a second, degenerate minimum appears, becoming the new global minimum. Due to thermal fluctuations, ϕ tunnels into the true vacuum, rendering a FOPT.

In chapter 5, we showed three plots (see Figs. 5.1–5.3) of the computed stochastic GW spectra for different masses μ, gauge couplings g, and self couplings λ. We fixed two parameters in each plot and varied the remaining parameter to analyze the behavior of peak frequency f_{peak}, peak amplitude $h^2\Omega_{\text{GW}}^{\text{peak}}$, PT strength α and inverse PT timescale $\frac{\beta}{H}$ for different parameter values. The GW signals depend strongly on the gauge coupling since we observe significant changes in peak frequency and peak amplitude for rather small changes in g (cf. Tabs. 5.1–5.3). Furthermore, we found that peak frequency, peak amplitude and PT strength were comparatively small affected by variations in self coupling and that the PT happens more slowly for lager λ. Faster PTs take place for small masses and small gauge couplings. Moreover, we also noticed that PTs are stronger for smaller masses and for larger gauge couplings.

So far none of the computed GW signals reaches into the PLI curve of the Einstein Telescope. One possible next step would be to find parameter values for μ, g and λ such that the GW signal falls within the ET detection range. Furthermore, it would be interesting to investigate the found parameter space for perturbativity and whether α and β are suitable to enable such PTs.

Since with daisy resummation (cf. Eq. 3.17), large uncertainties enter the GW spec-

tra, a more robust perturbative approach should be chosen in using high-temperature effective theories for thermal resummation [10].

Appendix A
A minimal model

We consider a pure, real scalar field model with positive mass parameter μ^2 that only couples to itself. The Euclidean Lagrangian density reads [33]

$$\mathcal{L}_E = \frac{1}{2}\partial_\mu\phi\,\partial_\mu\phi - \frac{\mu^2}{2}\phi^2 + \frac{\lambda}{4}\phi^4\,, \tag{A.1}$$

with the same tree-level potential as in Eq. (3.6). The thermal effective potential is constructed as described in Eqs. (3.12) – (3.17) with the parameter values listed in the first column of Tab. 3.1. However, as mentioned in [27], a cubic term in $V_{\text{tree}}(\phi)$ is required to generate a tree-level barrier.

The temperature-dependent evolution of the thermal effective potential is displayed in Fig. A. No barrier is generated due to radiative or thermal corrections. As tem-
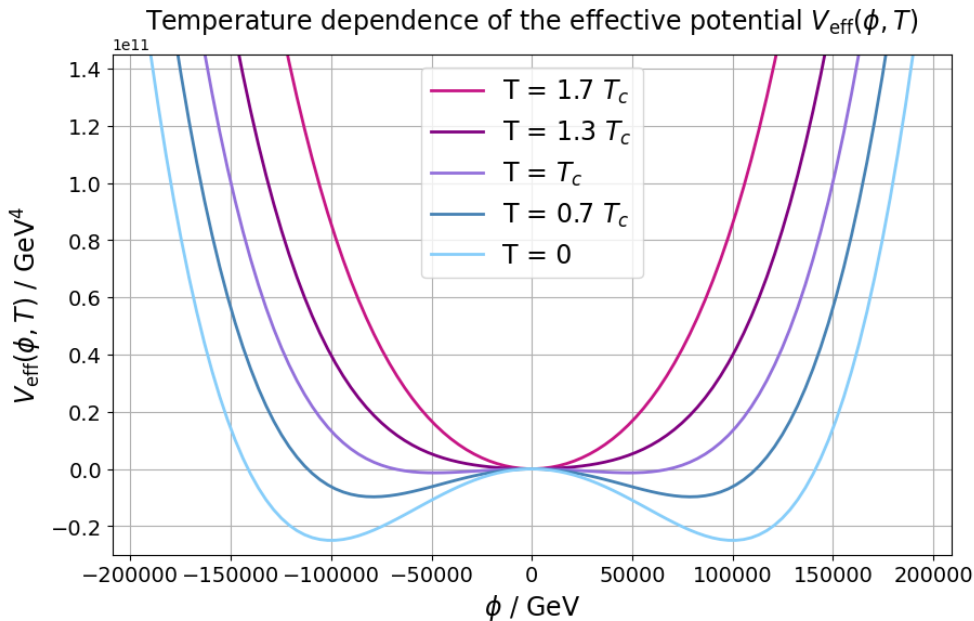

Fig. A.1: Thermal effective potential $V_{\text{eff}}(\phi, T)$ (cf. Eq. 3.12 – 3.17) in a pure, real scalar field model with m $= \sqrt{10}$ GeV and $\lambda = 10^{-9}$.

peratures drops, the global minimum slowly transforms into a local maximum with

no thermal barrier being created in the process. During this continuous transition, the scalar field immediately acquires a VEV at critical temperature T_c and smoothly "rolls down" the potential. As no thermal barrier has to be overcome, no latent heat is released in this process. In that case, the PT is of second or higher order[1] and there will be no bubble formation and consequently no generation of GWs through their collision, sound wave propagation or MHD turbulences.

---

[1]For second-order PTs, the discontinuity of the free energy density at critical temperature occurs in the second-order derivative, and so forth.

ACKNOWLEDGEMENTS

Bibliography

[1] `https://github.com/clwainwright/CosmoTransitions/blob/master/cosmoTransitions/tunneling1D.py`.

[2] P. Arnold and O. Espinosa, *Effective potential and first-order phase transitions: Beyond leading order*, Physical Review D **47** (1993), 3546–3579.

[3] S. Babak, J. Gair, A. Sesana, E. Barausse, C. F. Sopuerta, C. P. L. Berry, E. Berti, P. Amaro-Seoane, A. Petiteau, and A. Klein, *Science with the space-based interferometer LISA. v. extreme mass-ratio inspirals*, Physical Review D **95** (2017), no. 10.

[4] D. Baumann, *Lecture on cosmology*, `http://cosmology.amsterdam/education/cosmology`.

[5] _____, *Lecture on general relativity*, `http://cosmology.amsterdam/wp-content/uploads/2021/10/GR-Oct19.pdf`.

[6] M. Breitbach, *Gravitational waves from cosmological phase transitions*, 2022.

[7] M. Breitbach, J. Kopp, E. Madge, T. Opferkuch, and P. Schwaller, *Dark, Cold, and Noisy: Constraining Secluded Hidden Sectors with Gravitational Waves*, Journal of Cosmology and Astroparticle Physics **2019** (2019), no. 7.

[8] C. G. Callan and S. Coleman, *Fate of the false vacuum. ii. first quantum corrections*, Physical Review D **16** (1977), 1762–1768.

[9] S. Coleman, *Fate of the false vacuum: Semiclassical theory*, Physical Review D **15** (1977), no. 10, 2929–2936.

[10] D. Croon, O. Gould, P. Schicho, T. V. I. Tenkanen, and G. White, *Theoretical uncertainties for cosmological first-order phase transitions*, Journal of High Energy Physics **2021** (2021), no. 4.

[11] D. Curtin, P. Meade, and H. Ramani, *Thermal resummation and phase transitions*, 2016.

[12] A. Das, *Finite Temperature Field Theory*, 2. ed., World Scientific Publishing, 2023.

[13] A. Einstein, *Approximative integration of the field equations of gravitation*, Sitzungsber. Preuss. Akad. Wiss. Berlin (Math. Phys.) (1916), 688–696.

[14] ———, *Über Gravitationswellen*, Sitzungsber. Preuss. Akad. Wiss. Berlin (Math. Phys.) (1918), 154–167.

[15] J. Ellis, M. Lewicki, and J. M. No, *On the maximal strength of a first-order electroweak phase transition and its gravitational wave signal*, Journal of Cosmology and Astroparticle Physics **2019** (2019), no. 04, 003–003.

[16] J. Ellis, M. Lewicki, and V. Vaskonen, *Updated predictions for gravitational waves produced in a strongly supercooled phase transition*, Journal of Cosmology and Astroparticle Physics **2020** (2020), no. 11, 020–020.

[17] F. Englert and R. Brout, *Broken Symmetry and the Mass of Gauge Vector Mesons*, Physical Review Letters **13** (1964), 321–323.

[18] A. Afzal et al., *The NANOGrav 15 yr Data Set: Search for Signals from New Physics*, The Astrophysical Journal Letters **951** (2023), no. 1.

[19] A. Sesana et al., *Unveiling the gravitational universe at μ-Hz frequencies*, Experimental Astronomy **51** (2021).

[20] B. P. Abbott et al., *Observation of gravitational waves from a binary black hole merger*, Physical Review Letters **116** (2016), no. 6 061102.

[21] C. Caprini et al., *Science with the space-based interferometer eLISA. II: Gravitational waves from cosmological phase transitions*, JCAP **1604** (2016), no. 04 001.

[22] G. Aad et al., *Observation of a new particle in the search for the Standard Model Higgs boson with the ATLAS detector at the LHC*, Physics Letters B **716** (2012), no. 1, 1–29.

[23] M. Punturo et al., *The Einstein Telescope: a third-generation gravitational wave observatory*, Class. Quantum Grav. **27** (2010), no. 19.

[24] N. Aghanim et al., *Planck 2018 results*, Astronomy & Astrophysics **641** (2020), A6.

[25] P. A. R. Ade et al., *Planck 2015 results. XIII. Cosmological parameters*, Astronomy & Astrophysics **594** (2016), A13.

[26] S. L. Glashow, *Partial-symmetries of weak interactions*, Nuclear Physics **22** (1961), 579–588.

[27] O. Gould, *Real scalar phase transitions: a nonperturbative analysis*, Journal of High Energy Physics **2021** (2021), no. 4.

[28] G. S. Guralnik, C. R. Hagen, and T. W. B. Kibble, *Global Conservation Laws and Massless Particles*, Physical Review Letters **13** (1964), 585–587.

[29] P. W. Higgs, *Broken Symmetries and the Masses of Gauge Bosons*, Physical Review Letters **13** (1964), 508–509.

[30] M. Hindmarsh, M. Lüben, J. Lumma, and M. Pauly, *Phase transitions in the early universe*, SciPost Phys. Lect. Notes (2021), 24.

[31] J.Crowder and N. J. Cornish, *Beyond LISA: Exploring future gravitational wave missions*, Physical Review D **72** (2005), no. 8.

[32] A. Kosowsky, M. S. Turner, and R. Watkins, *Gravitational radiation from colliding vacuum bubbles*, Physical Review D **45** (1992), 4514–4535.

[33] M. Laine and A. Vuorinen, *Basics of Thermal Field Theory*, Springer International Publishing, 2016.

[34] A. D. Linde, *Decay of the False Vacuum at Finite Temperature*, Nuclear Physics B **216** (1983), no. 2, 421–445.

[35] M. Malinský, *Fun with the Abelian Higgs model*, The European Physical Journal C **73** (2013), no. 5.

[36] A. L. Maroto and J. Ramirez, *A Conceptual Tour About the Standard Cosmological Model*, 2004.

[37] A. A. Michelson and E.W. Morley, *On the relative motion of the earth and the luminiferous ether*, American Journal of Science **s3-34** (1887), no. 203, 333–345.

[38] K. Nguyen, *The Higgs Mechanism*, 2009, `https://www.theorie.physik.uni-muenchen.de/lsfrey/teaching/archiv/sose_09/rng/higgs_mechanism.pdf`.

[39] E. M. Pimentel, *Phenomenology of new physics models at colliders and in gravitational waves*, Ph.D. thesis, Johannes Gutenberg-Universität Mainz, 2020.

[40] L. Reina, *TASI 2011: Lectures on Higgs-Boson Physics*, 2012.

[41] A. Salam and J. C. Ward, *Weak and electromagnetic interactions*, II Nuovo Cimento (1955-1965) **11** (1959), 568–577.

[42] B. F. Schutz and F. Ricci, *Gravitational Waves, Sources, and Detectors*, 2010.

[43] E. Thrane and J. D. Romano, *Sensitivity curves for searches for gravitational-wave backgrounds*, Physical Review D **88** (2013), no. 12.

[44] C. L. Wainwright, *CosmoTransitions: Computing cosmological phase transition temperatures and bubble profiles with multiple fields*, Computer Physics Communications **183** (2012), no. 9, 2006–2013.

[45] S. Weinberg, *A Model of Leptons*, Physical Review Letters **19** (1967), 1264–1266.